Dalton Transactions

Accepted Manuscript

ROYAL SOCIETY OF CHEMISTRY

www.rsc.org/dalton

Mechanism of Water Oxidation by Non-Heme Iron Catalysts when Driven with Sodium Periodate

Alexander R. Parent,[a*] Takashi Nakazono,[b] Shu Lin,[b] Satoshi Utsunomiya[b] and Ken Sakai[a,b,c*]

Received (in XXX, XXX) Xth XXXXXXXXX 20XX, Accepted Xth XXXXXXXXX 20XX
DOI: 10.1039/b000000x

ABSTRACT Iron tris(2-methylpyridyl)amine (TPA) and iron 1-(bis(2-methylpyridyl)amino)-2-methyl-2-propanoate (BPyA) salts are characterized as water oxidation catalysts (WOCs) using sodium periodate. Under the conditions used, these complexes serve as homogeneous WOCs as demonstrated via kinetic analysis and dynamic light scattering (DLS). The Fe(BPyA) salt serves as both a mononuclear and dinuclear catalyst, with the mononuclear form showing higher catalytic activity. Based on the H/D kinetic isotope effect and pH dependence, the rate determining step (RDS) in water oxidation (WO) by Fe(BPyA) is nucleophilic attack by water during O-O bond formation. In contrast, Fe(TPA) shows complex kinetic behavior due to the formation of multiple oxidation states of the complex in solution, each of which exhibits catalytic activity for WO. The RDS in WO by Fe(TPA) follows an equilibrium established between monomeric and dimeric forms of the catalyst. Under acidic conditions formation of the monomer is favored, which leads to an increase in the WO rate.

1. Introduction

Water oxidation (WO) as a method of generating solar fuels has been a major focus of research in inorganic and organometallic chemistry in the past decade, prompted by increased awareness of the costs of consuming fossil fuels and releasing carbon dioxide into the atmosphere.[1] A number of highly active water oxidation catalysts (WOCs) based on second and third row transition metals have been reported, particularly using Ru[2–12] and Ir.[13,14] In order to enable the rapid and widespread adoption of solar water splitting as an alternative to fossil fuels, WOCs based on abundant first row transition metals are greatly desirable. Nevertheless, development of WOCs using first row transition metals has proven challenging, despite considerable efforts and some early successes in the field.[15–17] Those which have been developed focus mainly on Co[18–21] and Mn.[15,22–25]

Recently the Bernhard group reported the first Fe-based WOC.[26] Shortly after this report a family of 4-N non-heme Fe complexes were reported as WOCs when driven with cerium(IV) ammonium nitrate (CAN) and $NaIO_4$ by the Lloret-Fillol and Costas groups.[27] Although these catalysts were shown to be homogeneous under acidic conditions when using CAN, further studies showed that they form iron oxide nanoparticles when driven using $Ru(bpy)_3^{2+}$ and $S_2O_8^{2-}$ under neutral to alkaline pH, which then serve as the WOC under those conditions.[28] The formation of these nanoparticles is attributed to the higher pH at which the experiments were performed. The pH dependence on nanoparticle formation by these WOCs has been further characterized by the Fukuzumi group,[29] and very recently the Sun group has reported on this family of catalysts.[30]

The WO mechanism of these catalysts remains contentious. In addition to the rate determining oxidation process proposed in the original report,[27] an all Fe(IV) catalytic cycle has been proposed based on computation.[31] In their follow-up report, the Lloret-Fillol and Costas groups have proposed that the rate determining step (RDS) of WO by these catalysts when driven with CAN is O-O bond formation preceded by formation of a hydroxide bridged iron cerium adduct.[32] This mechanism was then further refined using DFT calculations.[33] More recently the mononuclear nature of the catalysts has come into question, with a dimeric precursor found to give a higher rate than the monomer under certain conditions.[34] On the other hand, mechanistic insights obtainable using sodium periodate have been relatively unexplored, despite its reported ability to drive WO with these WOCs in the initial report.[27]

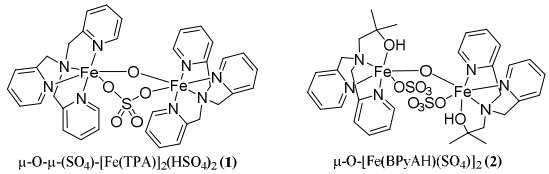

Fig. 1 Complexes studied in this work. Bisulfate counteranions omitted from **1** for clarity.

Use of sodium periodate has allowed for the improved characterization of a number of Ir-based WOCs due to its relatively low overpotential and the wide pH range over which it functions.[35–42] However, care must be taken when using sodium periodate to drive WO, as it can easily serve as an oxo-transfer agent, and in theory could serve as the sole source of any oxygen production observed.[43,44] Nevertheless, careful study with sodium periodate allows for a more thorough understanding of the catalytic mechanism of WOCs, in turn aiding the design of WOCs with improved reactivity and stability.[38] In this manuscript, we report that the non-heme Fe complexes **1** and **2** (Fig. 1) serve as homogeneous WOCs, and propose mechanisms for WO by these complexes when driven with sodium periodate.

2. Experimental Methods

2-Pyridinecarboxaldehyde, 1-amino-2-methyl-2-propanol, 2-(chloromethyl)pyridine hydrochloride, and tris(2-methylpyridyl)amine (TPA) were purchased from Tokyo Chemical Industry Co., Ltd. and used without further purification. Iron(II) sulfate was purchased from Kokusan Chemical Co., Ltd.

and used as received. Hydrogen peroxide (35%) was purchased from Tokyo Chemical Industry Co., Ltd. and its concentration was determined via titration with potassium permanganate purchased from Kanto Chemical Co., Inc. prior to use. Sodium cyanoborohydride and iron(III) sulfate hydrate were purchased from Sigma-Aldrich Co. and were not further purified. Deuterated solvents were purchased from Sigma-Aldrich Co. or Wako Pure Chemical Industries, Ltd. and used as received. NMR spectra were recorded on a 600 MHz JEOL spectrometer and referenced to TMS. UV-Visible spectra were recorded on a Shimadzu UV2450SIM spectrophotometer. EPR data were acquired on a JEOL JES-FA200 spectrometer at room temperature in aqueous solution using a flat cell. Spectral data fitting was performed using the SPECFIT software package.[45] Elemental analysis was performed by the Kyushu University Faculty of Sciences Center for Elemental Analysis. A YSI 5300A Clark-type electrode was used to measure changes in dissolved oxygen concentration for kinetic analysis. Electrospray ionization mass spectra were obtained on a JEOL JMS-T100LC mass spectrometer in positive ion mode. Mass spectra were simulated using WinMassSpec.[46] The pH of the solutions was measured using a TOA-DKK HM-20J pH meter. pD was calculated using the approximation pD = pH + 0.4.[47] Solutions were adjusted to the reported pH values using 5 mM (10 mN) sulfuric acid and 10 mM sodium hydroxide.

Synthesis of BPyAH

1-(Bis(2-methylpyridyl)amino)-2-methyl-2-propanol (BPyAH) was synthesized via reductive amination based on the procedure reported by Groves and Kady for bis(2-methylpyridyl)methylamine.[48] Sodium cyanoborohydride (730 mg, 11.6 mmol) and 1.1 mL 2-pyridinecarboxaldehyde (11.6 mmol) were dissolved in 10 mL of methanol. Separately, 0.67 mL of glacial acetic acid (11.6 mmol) and 0.5 mL of 1-amino-2-methyl-2-propanol were added to 10 mL of methanol. The 1-amino-2-methyl-2-propanol solution was then slowly added to the cyanoborohydride solution and was stirred for two days. The solvent was then removed under reduced pressure, and the solid was re-dissolved in 10 mL of water and adjusted to pH 9 with sodium hydroxide. The aqueous solution was extracted three times with 20 mL of dichloromethane, and the organic fractions were combined and dried with magnesium sulfate. After reducing the volume under reduced pressure, the organic phase was passed through a silica column with 5% methanol in ethyl acetate, the product containing fractions were combined, and the solvent was removed under reduced pressure to yield 913.4 mg of light yellow oil (3.4 mmol, 58% yield) which was stored in a freezer. Calculated for hemihydrate: C 68.54, H 7.91, N 14.99; Found: C 69.09, H 7.65, N 14.94.

Synthesis of μ-O-μ-(SO_4)-[(TPA)Fe]$_2(HSO_4)_2$ · MeOH (1)

To a solution of $Fe_2(SO_4)_3$ · n H_2O (n not known) (89.8 mg) in 1 mL water were added a solution of 102.6 mg (0.3 mmol) TPA in 2 mL 1:1 water:acetonitrile and one drop of 1 M H_2SO_4. The solution rapidly changed dark green, and was evaporated to dryness under reduced pressure. Recrystallization via vapor diffusion of diethyl ether into a methanol solution afforded a sample of sufficient purity to pass elemental analysis and for X-ray diffraction studies (112.4 mg, 0.1 mmol, 33% yield). Calculated: C 43.12, H 4.11, N 10.87; Found: C 42.14, H 4.30, N 10.53.

Synthesis of μ-O-[(BPyAH)Fe$(SO_4)]_2$ · MeOH · 2H_2O (2)

To a solution of 109.8 mg BPyAH (0.401 mmol) in 1 mL water was added 97.1 mg iron(II) sulfate heptahydrate (0.349 mmol). After stirring for 4 h under air, the solution was evaporated to dryness under reduced pressure and the residue was redissolved in 10 mL of dichloromethane. The solution was filtered and the filtrate was evaporated under reduced pressure yielding 119.8 mg of brown powder (0.235 mmol, 67 % yield). Recrystallization of it from methanol/diethyl ether afforded crystals of μ-O-[(BPyA)HFe$(SO_4)]_2$ · 2.5 H_2O · 4 MeOH (**2b**) suitable for X-ray diffraction studies, which upon drying yielded **2**. Calculated: C 42.59, H 5.42, N 9.03; Found: C 42.64, H 5.16, N 9.26.

General Procedure for Clark Electrode Measurements

A solution of sodium periodate (5.00 mL) was placed in the electrode chamber, which was then sealed such that no headspace remained. Solutions were not deaerated prior to use. After the baseline had stabilized, concentrated catalyst solution was injected into the electrode chamber while stirring, and the change in electrode current over time was recorded. The initial rate was determined based on the slope of [O_2] vs. time for approximately the first two min of the reaction after the induction period (when present). This procedure was repeated a minimum of three times per reaction condition.

Procedure for Electrochemical Measurements

Samples were dissolved in a 100 mM KNO_3 electrolyte solution yielding a final catalyst concentration of 0.50 mM. Data was collected at a 100 mV/s scan rate with a constant Ar purge. A three electrode cell was used with a glassy carbon, platinum wire, and saturated calomel electrode used as working, counter, and reference electrodes respectively.

Crystallography

Crystals were mounted on fiberglass using Paratone oil and cooled to 100 K in a stream of cold N_2 gas. Diffraction data were collected using a Bruker SMART APEXII CCD area detector diffractometer with the detector positioned at a distance of 6.0 cm from the crystal. The X-ray source was monochromated Mo-Kα radiation (λ = 0.71073 Å) from a rotating anode with a mirror focusing apparatus operating at 1.2 kW (50 kV, 24 mA). Corrections for absorption were made by SADABS.[49] The structures were solved by the direct method using SHELXS-97,[50] and refined anisotropically on F^2 with SHELXL-97.[51] For **1**, all hydrogen atoms except for those of the methyl group of methanol were refined isotropically, while those of the methyl group were placed in idealized positions (methyl C-H = 0.98 Å) and included in the refinement in a riding-model approximation. For **2**, all H atoms were similarly placed in idealized positions (methyl C-H = 0.96 Å, methylene C-H = 0.97 Å, and aromatic C-H = 0.93 Å), except for those of the solvent water and disordered methanol, which were not located. ORTEP diagrams were generated using ORTEPII[52] and TEXSAN.[53]

Procedure for Dynamic Light Scattering Analysis

Concentrated catalyst solution was added to a solution of sodium

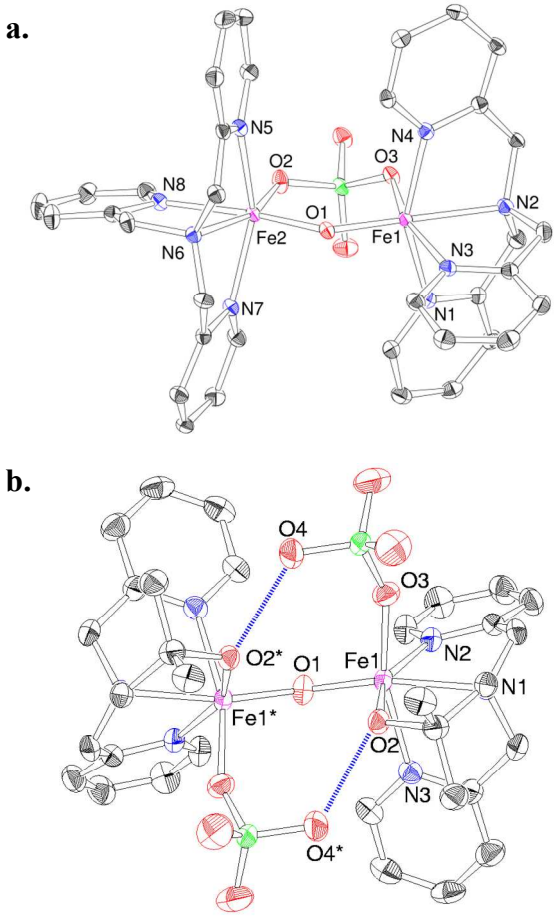

Fig. 2 Thermal ellipsoid plots of the molecular units of **1** (a.) and **2b** (b.) showing 50% probability ellipsoids; hydrogen atoms, lattice solvent molecules and counteranions omitted for clarity. Blue dashed line shows location of H-bonds in **2b** Color coding: Blue, N; Red, O; Black, C; Purple, Fe; Green, S.

periodate, and analyzed with an ELSZ-2 (Otsuka Electronics Co. Ltd. Japan) using a He laser operating at 660 nm.

Procedure for ESI-MS Titration

Small aliquots of a solution of 20.3 mM sodium periodate were added to 20.0 mL of a 313 μM aqueous solution of **1**, and a 50 μL aliquot of the resultant solution was diluted with 1 mL of acetonitrile prior to injection into the spectrometer.

Procedure for HAADF-STEM Measurements

High-angle annular dark-field scanning transmission electron microscopy (HAADF-STEM) and STEM energy dispersive X-ray analysis were performed using a JEOL ARM200F equipped with double Cs correctors. The acceleration voltage was 200 kV. The probe size of the electron beam was ~1.0 Å in STEM mode. Drift correction was used in the STEM elemental mapping. Sample solutions were prepared by injecting 20.0 μL of 25.1 mM $Fe(NO_3)_3$ into 5.0 mL of 10.0 mM sodium periodate, and aging for ~30 minutes. A droplet of the sample solution was then passed through a porous carbon mesh on 3 mmϕ TEM copper grid.

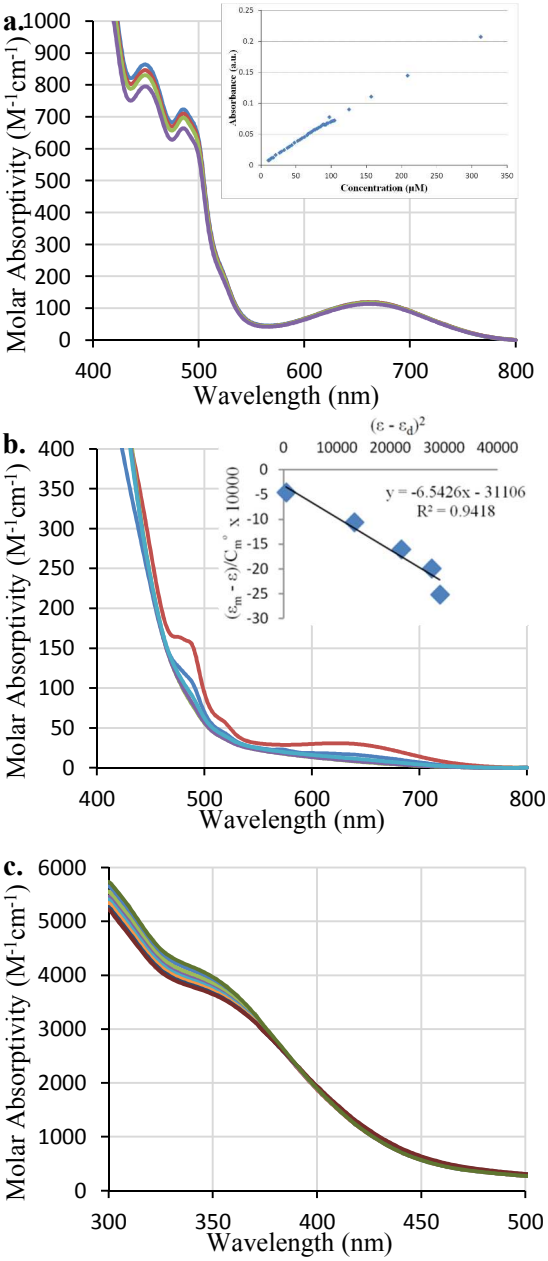

Fig. 3 Visible spectra of (a.) 125, 157, 209 and 313 μM **1**, with inset showing absorbance at 486 nm vs. the concentration of **1**, (b.) 164, 218, 326, 655 and 2570 μM **2** at pH 3.7, with inset showing linear fit to $(\varepsilon_m - \varepsilon)/C_m° $ vs. $(\varepsilon - \varepsilon_d)^2$ at 487 nm and (c.) 489, 443, 404, 372, 310, 266, 233, 207, and 186 μM **2** at pH 4.7 showing isosbestic point at ~390 nm. Spectra in (a.) and (b.) were adjusted to zero absorbance at 800 nm.

3. Results

3.1 Structural Properties of μ-O-μ-(SO_4)-$[(TPA)Fe]_2(HSO_4)_2 \cdot$ MeOH (1) and μ-O-$[(BPyAH)Fe(SO_4)]_2 \cdot 2H_2O$ (2)

The structural parameters for **1** and **2b** were determined by X-ray diffraction, and a graphical representation of these complexes is shown in Fig. 2. The Fe-O(oxo) bond lengths in **1** (1.792 and 1.806 Å) are very similar to those previously reported for the perchlorate salt, μ-O-μ-(SO_4)-$[Fe^{III}(TPA)]_2(ClO_4)_2 \cdot 0.75MeCN \cdot 0.25H_2O$ (1.788 and 1.807 Å),[54] consistent with the assignment of

1 as a μ-oxo, μ-sulfato-bridged Fe(III,III) dimer. The Fe-O-Fe bond angle in **1** (134.34°) is slightly larger than that in the perchlorate analogue (133.03°), and the Fe-O(sulfate) bond distances are slightly longer in **1** (1.964 and 2.022 Å) than in the perchlorate salt (1.950 and 2.012 Å).[54]

Complex **2** crystallizes with methanol lattice solvents (**2b)** in the Pbcn space group, with the bridging oxo located on the two-fold symmetry axis. A hydrogen bonding interaction exists between the alcoholic proton and the sulfate anion, with the O(alcohol)-O(sulfate) bond length found to be 2.562 Å. The bond length between the Fe and bridging oxo is 1.788 Å, which is quite consistent with the bond lengths reported for the related complex μ-O-[Fe(HPCINOL)(SO_4)]$_2$ · 6H_2O (HPCINOL = 1-(bis-pyridin-2-ylmethyl-amino)-3-chloropropan-2-ol; Fe-O(oxo) = 1.777 and 1.794 Å).[55] Unlike in the HPCINOL complex, the sulfate molecule in **2b** is bound cis rather than trans to the alcohol, resulting in a shorter Fe-O(alcohol) bond length in **2b** (2.035 Å vs. 2.135 and 2.144 Å). As with the HPCINOL complex, a disordered solvent site is found in the crystal structure.

In order to determine whether **1** and **2** remain dimeric in solution, their visible absorption spectra as a function of concentration were measured. For **1**, no variation in molar absorptivity is observed upon changing the concentration (Fig. 3a), with the metal oxo charge transfer bands at 450 and 480 nm clearly visible at low concentrations as seen in similar Fe(III,III) oxo-bridged species.[56] Spectral changes as a function of pH were measured for **1** by titration with 10 mM sodium hydroxide. The initial pH of the solution was measured to be 3.01, consistent with the presence of the two HSO_4^- counter anions in the crystal lattice (pH 2.99 for 1.04 mM H^+). A single pK_a of 6.4 was found for **1**, likely due to deprotonation of a bound aqua (Figs. S5-6). No other spectral changes are observed over the pH range assayed (3-8.5). These data indicate that **1** remains entirely dimeric under the concentration and pH regimes studied.

In contrast, **2** exhibits distinct changes in absorption with varying concentration (Fig. 3b). Charge transfer bands similar to those seen for **1** are only seen for **2** at high concentrations. This result indicates an equilibrium between dimeric and monomeric forms of **2** in solution. In order to determine the equilibrium constant for dissociation, K_d, the spectral data was first modeled using SPECFIT (Fig. S7), yielding log(K_d) = -3.5 ± 0.7. This value was then confirmed at single wavelengths by plotting $(\varepsilon_m - \varepsilon)/C_m^\circ$ vs. $(\varepsilon - \varepsilon_d)^2$, which gives a linear function with a slope equal to $-2K_d/(\varepsilon_m - \varepsilon_d)$ (Equation 1), where ε_m and ε_d are the molar

$$\frac{\varepsilon_m - \varepsilon}{C_m^\circ} = \frac{-2K_d}{\varepsilon_m - \varepsilon_d}(\varepsilon - \varepsilon_d)^2 \qquad (1)$$

extinction coefficients calculated for the monomer and dimer, respectively, C_m° is the total concentration in terms of monomer, and ε is the measured molar extinction coefficient in terms of C_m°.[57] Fitting in this manner yields log(K_d) values of -2.9, -3.2 and -2.3 at 487, 518 and 632 nm, respectively (Figs. 3b insert and Figs. S8-9).

Further confirmation that only two species are involved in the spectral changes observed is the presence of an isosbestic point at ~390 nm (Fig. 3c). A model-free elementary factors analysis (EFA) of the spectra shown in Fig. 3c indicates that the equivalence point occurs when the concentration of **2** is ~430 μM (~860 μM monomer basis). This is equivalent to a log(K_d) value

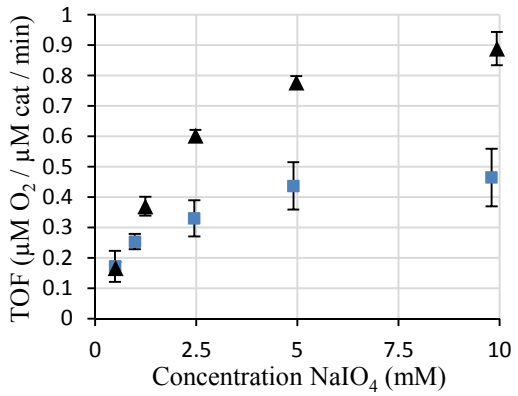

Fig. 4 Initial turnover frequency vs. periodate concentration for 32.2 μM **1** (squares) and 13.0 μM **2** (triangles) at pH 5.0. Error bars represent two standard deviations from the mean.

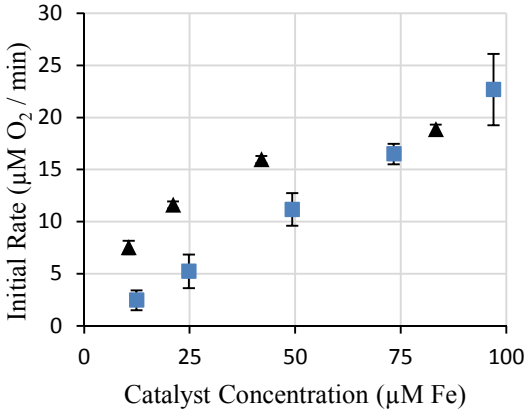

Fig. 5 Initial WO rate vs. catalyst concentration (Fe basis) for **1** (squares) and **2** (triangles) in 10 mM sodium periodate at pH 5.0. Error bars represent two standard deviations from the mean.

of -3.54. The K_d values calculated by these three methods are in good agreement. Taking a value of $10^{-3.5}$ for K_d, ~93% of **2** is monomeric under the conditions used for the kinetic studies ([**2**] = 13.0 μM, Section 3.5).

3.2 Kinetic Characterization of WO by μ-O-μ-(SO_4)-[(TPA)Fe]$_2$(HSO_4)$_2$ · MeOH (1) with Sodium Periodate

We first endeavored to determine whether sodium periodate can be used to drive WO with **1** by measuring its WO rate under various periodate and catalyst concentrations (Figs. 4 and 5). As shown in Fig. 4, the WO rate of **1** saturates as the periodate concentration is increased, indicating that the reaction is zero-order with respect to periodate at high periodate concentrations. Any contribution from disproportionation of periodate to the observed O_2 (Equation 2) must therefore be minor, and the

$$2\ IO_4 \rightarrow 2\ IO_3 + O_2 \qquad (2)$$

kinetic and spectroscopic data obtained when driving WO by **1** with periodate can thus be employed to understand its WO mechanism.[35] Fig. 5 shows that the WO rate is first order with respect to the concentration of **1**, which in conjunction with Fig. 3a shows that **1** preserves its dimeric structure under these conditions.

Taking advantage of the constant overpotential provided by periodate between pH ~2 and ~7,[43] the WO rate of **1** was

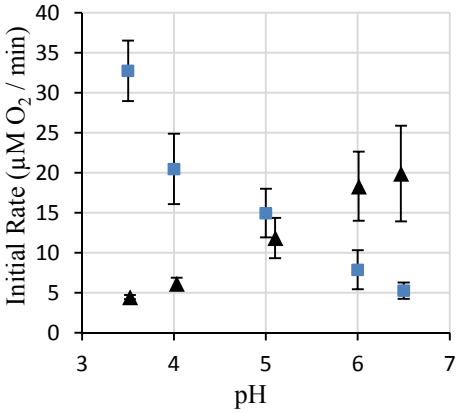

Fig. 6 Initial WO rate in 10 mM sodium periodate as a function of pH for 32.2 μM **1** (squares) and 13.0 μM **2** (triangles). Error bars represent two standard deviations from the mean.

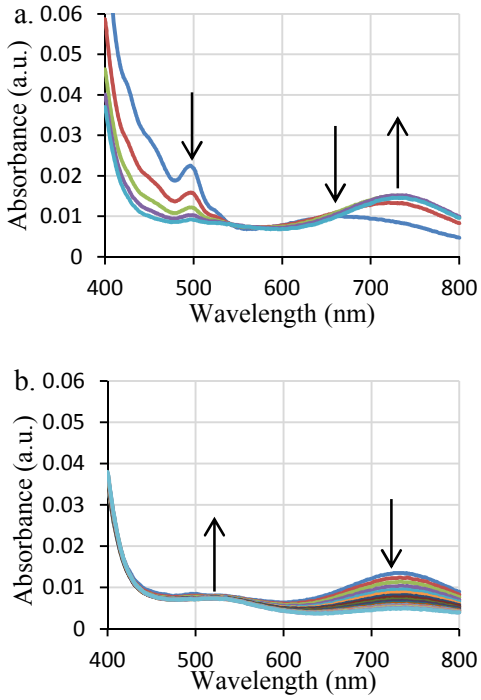

Fig. 7 Visible time course of the reaction of 48.5 μM **1** with 10.0 mM sodium periodate (pH 5.0) from (a.) 0-4 and (b.) 5-21 min. Data was collected at 1 min intervals; initial time-point corresponds to ~15 s after mixing. Arrows indicate direction of change with time.

$$A \xrightarrow{k_1} B \xrightarrow{k_2} C$$

Scheme 1 Model used to fit spectral changes in SPECFIT.

measured as a function of pH. As shown in Fig. 6, the WO rate increases dramatically as the pH is lowered. Due to the constant overpotential provided by periodate, thermodynamic effects on the WO rate can be excluded, indicating that the observed change in rate arises purely from kinetic factors. An increase in rate at acidic pH is extremely unusual for a WOC, as the RDS for WO is commonly either nucleophilic attack by water or oxo-oxo coupling,[16,58] during both of these mechanisms either protons are lost or there is no proton involvement. Such a rate enhancement has been observed for the blue dimer due to reduced anation at

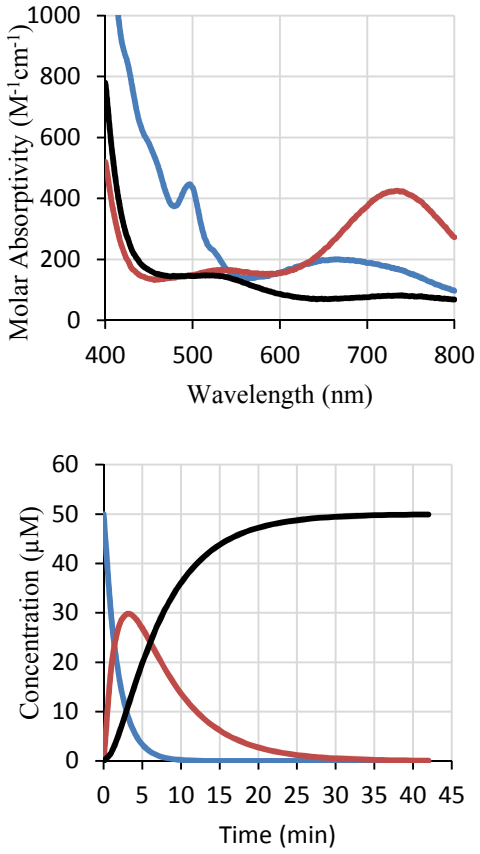

Fig. 8 Predicted absorption spectra (top) and concentration over time (bottom) for species **A** (blue), **B** (red), and **C** (black) resulting from the reaction of 48.5 μM **1** with 10.0 mM sodium periodate (pH 5.0).

low pH,[59] and upon addition of nitric acid due to its ability to enhance the reactivity of Ce(IV).[10,60] As discussed in Section 3.1, **1** has a pK_a of 6.4, which may explain the decrease in rate as the pH is increased from 5 to 6.5, but cannot explain the greatly enhanced rate under more acidic conditions. The observed pH dependence must therefore result either from a change in speciation with pH by species formed during WO by **1** or from a protonation as the RDS of WO by **1**.

To test whether a protonation is involved in the RDS of WO by **1**, the H/D kinetic isotope effect (KIE) of WO by **1** was measured in D_2O. The observed KIE is 0.85 ± 0.04 (10.0 mM periodate, 32.2 μM **1,** pH/pD 6.0). This secondary inverse KIE is somewhat unusual, but was previously seen for WOCs when either the RDS follows a pre-equilibrium[13] or when the oxidant is involved in deprotonation.[10] This secondary inverse KIE conclusively precludes a protonation as the RDS of WO by **1**.

3.3 Spectral Characterization of WO by μ-O-μ-(SO_4)-$[(TPA)Fe]_2(HSO_4)_2$ · MeOH (1) with Sodium Periodate

In order to study potential intermediates formed during WO, the visible spectrum of **1** was monitored during WO. As shown in Fig. 7, upon addition of **1** to a solution of sodium periodate a change in the spectral features is observed. Deconvolution of the visible spectral changes using SPECFIT reveals four species present in the solution. The abundances of the first three of these species can be well fit using the simple sequential model shown in Scheme 1 (Fig. 8). The fourth spectral component corresponds

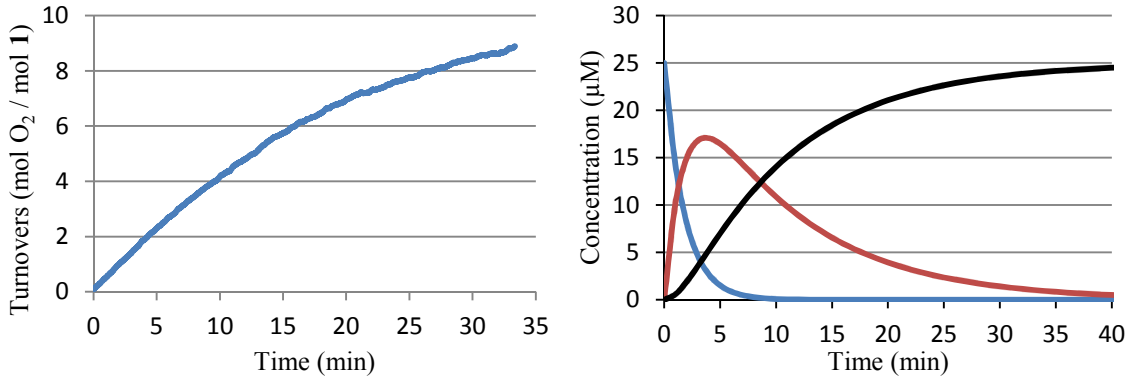

Fig. 9 Turnovers vs. time (left) and species concentrations vs. time predicted by spectral deconvolution (right) for the reaction of 24.7 μM **1** with 10.0 mM sodium periodate (pH 5.0).

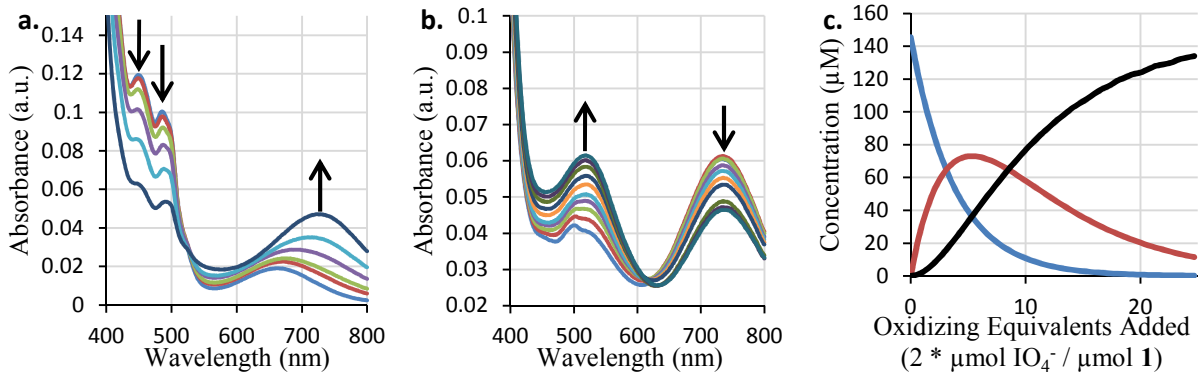

Fig. 10 (a.) Visible spectra of a 145 μM solution of **1** titrated with 9.75 mM $NaIO_4$ from 0 to 4 oxidizing equivalents added showing the first isosbestic point at ~ 520 nm, (b.) from 7.36 to 14 oxidizing equivalents showing the second isosbestic point at ~ 610 nm and (c.) concentrations of **1** (blue), **B** (red), and **C** (black) predicted using SPECFIT.

Table 1 Calculated pseudo-first order rate constants for the change in speciation during the reaction of **1** with $NaIO_4$.

[IO_4^-] mM	[**1**] (μM)	pH/pD	k_1 calc (**A** → **B**) (min^{-1})	k_2 calc (**B** → **C**) (min^{-1})
2.55	66.4	5.0	0.41 ± 0.04	0.131 ± 0.014
5.10	66.4	5.0	0.55 ± 0.05	0.143 ± 0.011
10.0	24.7	5.0	0.47 ± 0.04	0.127 ± 0.011
10.0	48.5	5.0	0.48 ± 0.04	0.205 ± 0.024
10.2	66.4	5.0	0.60 ± 0.03	0.195 ± .009
10.0	94.0	5.0	0.49 ± 0.06	0.32 ± 0.05
10.2	66.4	3.5	0.79 ± 0.01	0.102 ± 0.002
10.2	66.4	4.0	0.76 ± 0.02	0.124 ± 0.002
10.2	66.4	6.0	0.61 ± 0.02	0.209 ± 0.009
9.98*	66.4	6.0	0.47 ± 0.01	0.096 ± 0.002

* Run in D_2O.

to an overall increase in absorbance or scattering (Fig. S10), revealing the formation of nanoparticles as the reaction progresses. Nanoparticle formation at long time points was subsequently confirmed via DLS (Section 3.6).

The visible absorption of **A**, the initial species in the reaction mixture, differs slightly from that of **1** in solution (Fig. 3a), and corresponds to either an Fe(III,III) periodate adduct or another periodate modified species as it forms immediately upon mixing. The concentration of **A** as a function of time is well correlated with the absorption at 500 nm (Fig. 8). The calculated concentration of **B** is correlated with the absorption at 726 nm (Fig. 8) and its spectral features are similar to those which were previously assigned as Fe(IV) species in these systems.[27,32] Species **C** has a single weak absorption at ~ 530 nm (Fig. 8) and cannot be identified on the basis of its visible spectrum alone. Importantly, the charge transfer transition due to the bridging oxo in **1** is still present in **A**, indicating that the dimer remains intact during the initial phase of WO. Additionally, the calculated molar absorptivities of species **A**, **B** and **C** do not vary as a function of catalyst concentration or pH, suggesting that these species consist of a single component, or contain one major component which dominates the overall spectral features observed.

Table 1 shows the calculated pseudo-first order rate constants for WO by **1** under various conditions. By comparing the calculated rate constants for k_1, the conversion of **A** to **B** is found to be first order with respect to the catalyst concentration and saturates with respect to the periodate concentration as is observed for the WO rate (Fig. 4). In contrast to the first-order catalyst concentration dependence observed for k_1, the calculated rate constant for the conversion of **B** to **C**, k_2, increases is in the manner expected for a second order reaction; it shows a linear increase in the pseudo-first order rate constant with respect to catalyst concentration (Fig. S11), implying it is second order with respect to the concentration of **B**. Furthermore, the decrease in k_2 observed under acidic conditions and in deuterated solvent indicates that the formation of **C** involves loss of a proton.

Attempts to fit the spectral changes to a model incorporating a bimolecular reaction of **B** to form **C** were unsuccessful, indicating that the system is much more complicated than expected.

As shown in Fig. 9, the WO rate does not correlate well with any of the concentrations of **A**, **B** and **C**, with the maximum rate obtained reached within ~10 s and maintained for ~10 min. This lack of correlation indicates that species **A**, **B** and **C** are all competent WOCs, with **C** having reduced activity relative to **A** and **B**. In addition, the KIE for k_1 is found to be ~1.3 (Table 1), substantially larger than the value of 0.84 ± 0.04 determined for WO (Section 3.2). This difference in KIE suggests that rather than being an intermediate, **B** is formed from a branch in the catalytic cycle of WO by **A**. This conclusion is confirmed by the change in k_1 as a function of pH, which is much less dramatic than the change in the WO rate as a function of pH (Fig. 6 and Table 1).

In order to gain more insights into the natures of species **A**, **B** and **C**, a solution of **1** was titrated with sodium periodate. As shown in Fig. 10, species **B** and **C** can be generated by the slow addition of periodate, indicating that they are at least metastable under the conditions employed. Species **A,** on the other hand, does not form under these conditions, indicating an excess of periodate in solution is required for its formation from **1**. Species concentrations as a function of the oxidizing equivalents added were calculated using SPECFIT (Fig 10c). Interpretation of the titration equivalents required to form each species is not straightforward due to the fact that some of the periodate added is consumed by WO, for example ~ 2.5 oxidizing equivalents per Fe site are required to reach the maximum concentration of **B**. On the other hand, addition of small amounts of sodium periodate provides a convenient method for generating **B** and **C** in a reproducible and relatively long-lived manner, and enables their characterization with electrospray ionization mass spectrometry (ESI-MS) (Section 3.4).

Previous works showed that Fe(IV) and Fe(V) complexes are produced in the reaction of Fe(II) complexes with hydrogen peroxide.[61–63] In order to determine if **B** is generated via the formation of a hydroperoxo intermediate, a solution of **1** was mixed with H_2O_2 and the UV-Visible spectral changes were monitored using the stopped-flow technique. As shown in Fig. 11, no spectral changes are observed upon mixing H_2O_2 and **1**, despite rapid oxygen evolution under these conditions (Fig. S13). We thus rule out hydroperoxy and peroxo species, together with those derived from these species, as candidates for **B**.

3.4 ESI-MS Characterization of WO by μ-O-μ-(SO$_4$)-[(TPA)Fe]$_2$(HSO$_4$)$_2$ · MeOH (1) with Sodium Periodate

Given our ability to generate **B** and **C** from **1** via the addition of small amounts of periodate, we endeavored to identify these species using ESI-MS. Prior to addition of periodate, several peaks corresponding to Fe-containing species are observed (Fig. 12). The peaks at 514.9 and 555.9 m/z are consistent with the formulations [μ-O-(TPA)Fe$_2$(HSO$_4$)]$^+$ and [μ-O-(TPA)Fe$_2$(HSO$_4$)(MeCN)]$^+$, respectively (Figs. 13a,b and S14-15). The charge on these species indicates that they have an Fe(II,II) oxidation state, presumably due to reduction of them in the spectrometer. The small peaks at 496.9 and 537.9 m/z correspond to [μ-O-Fe$_2$(MeCN)$_9$]$^+$ and [μ-O-Fe$_2$(MeCN)$_{10}$]$^+$,

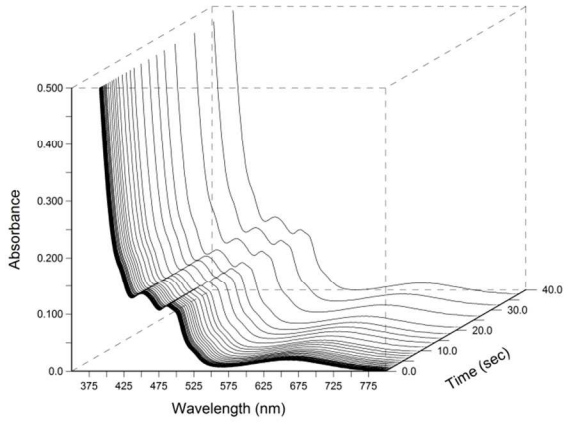

Fig. 11 Stopped-flow UV-Visible spectra upon reaction of 157 μM **1** with 9.76 mM H_2O_2, pH ~ 3.8.

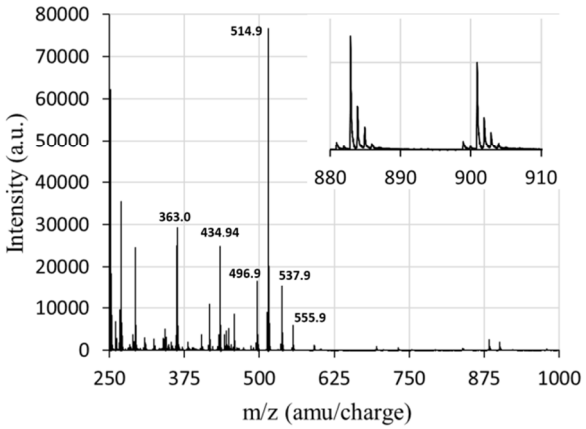

Fig. 12 ESI-MS of **1** after dissolution in water and addition to acetonitrile, inset shows expansion of region between 880 and 910 m/z. Free ligand (TPAH$^+$) appears at 291 m/z, compare to Fig. S3.

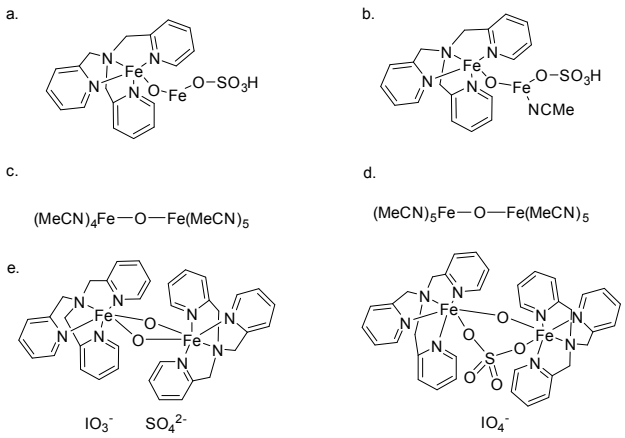

Fig. 13 Structures assigned to ESI-MS peaks at m/z 514.9 (a.), 555.9 (b.), 496.9 (c.), 537.9 (d.), and two possible structures for the peak at 994.9 (e.).

respectively. These possess a formally Fe(I,II) oxidation state (Figs. 13c,d and S16-17), similarly due to their reduction in the spectrometer. Ligand loss from the complex appears to be the result of ionization, as the same peaks are observed in the ESI-MS of **1** in MeOH (Fig. S3). The peaks at 434.9, 363.0, and 362.0 m/z correspond to [Fe(TPA)(OH$_2$)(NCMe)]$^+$, [Fe(TPA)(OH)]$^+$, and[Fe(TPA)(O)]$^+$, respectively. The small peak at 900.9 m/z

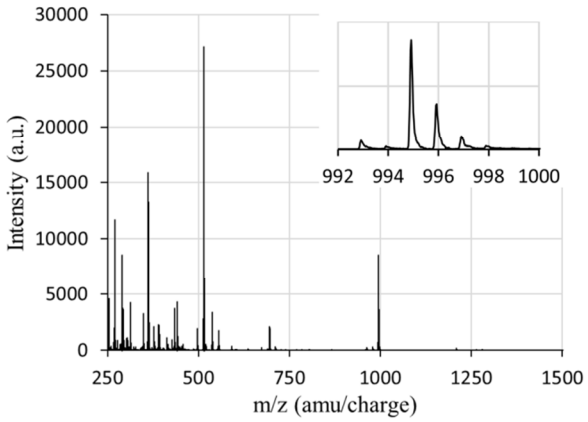

Fig. 14 ESI-MS of **1** after dissolution in water, addition of 18 equivalents of sodium periodate, and dilution with acetonitrile. Inset shows an expansion of the peak at m/z = 994.9.

corresponds to the parent complex in the Fe(III,III) oxidation state with a bisulfate counteranion, while the small peak at 882.9 m/z corresponds to a species given by loss of water from the former species.

Remarkably, during the course of the titration, only one new species is observed at 994.9 m/z (Figs. 14 and S18-29). This species begins to appear after adding six oxidizing equivalents to the solution and increases in intensity as additional oxidizing equivalents are added. Structural assignment of this peak is aided by its distinct isotope ratio, and reveals it to be either a di-μ-oxo-bridged Fe(TPA) dimer with one sulfate and one iodate counteranion in the Fe(IV,IV) oxidation state, or a mono-μ-oxo-bridged Fe(TPA) dimer with a (bound or unbound) sulfate and periodate counteranion in the Fe(III,III) oxidation state (Figs. 13e and S30). This peak can be assigned as species **C** on the basis of the spectrophotometric titration, which shows that only species **C** exists in solution after addition of more than ~25 oxidizing equivalents (Fig. 10).

As a mono-μ-oxo species in the Fe(III,III) oxidation state corresponds to the starting complex, it can be excluded as a candidate for **C**. Two possibilities thus remain; first **C** may be a di-μ-oxo Fe(IV,IV) dimer. Alternatively, **C** may correspond to a mono-μ-oxo dimer which is reduced to the Fe(III,III) species in the spectrometer. In combination with the visible spectra of **C** (Fig. 8), which shows similarities to nitride-bridged Fe(IV,IV) dimers,[64] we assign **C** as an Fe(IV,IV) dimer with either one or two μ-oxo bridges, or a mixture of these two species.

3.5 Characterization of WO by μ-O-[(BPyAH)Fe(SO$_4$)]$_2$ · MeOH · 2H$_2$O (2) with Sodium Periodate

In order to further study the mechanism of WO by this family of WOCs, we designed the BPyA ligand to provide a strongly basic alkoxide O-donor. This alkoxide donor was expected to stabilize higher oxidation states of the complex and thus provide both a better chance for characterization and kinetic data more easily interpreted than found for **1**. Consistent with our expectations, the Fe(II/III) couple for **2** shows a cathodic shift of ~40 mV relative to **1** (Fig. 15). Unexpectedly, an irreversible wave is visible in the cyclic voltammogram (CV) of **2** at ~770 mV vs. SCE, which appears to correspond to oxidation of the BPyA ligand (Fig. S31). Although much less pronounced a similar ligand-based oxidation is present in the CV of **1** at ~840 mV vs. SCE.

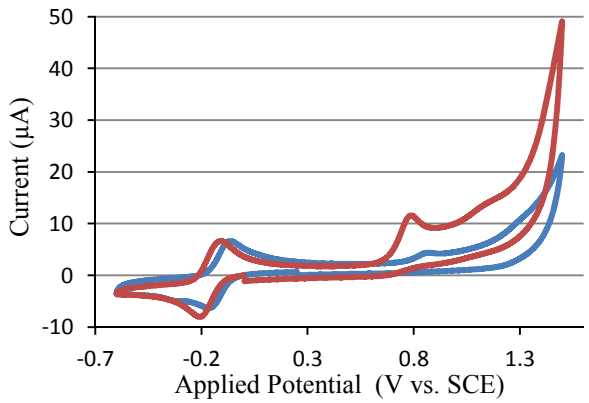

Fig. 15 Cyclic voltammograms of 500 μM **1** (blue) and **2** (red), under Ar atmosphere in 100 mM aqueous phosphate buffer at pH 6.8.

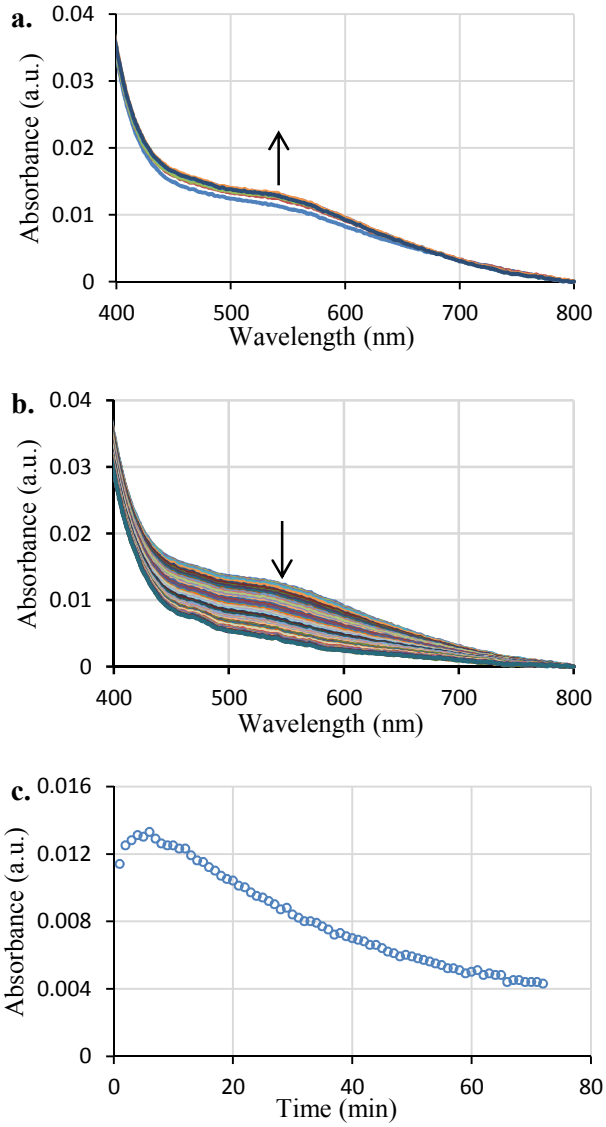

Fig. 16 Visible time-course of the reaction of 55.9 μM **2** with 10.2 mM sodium periodate at pH 5.0 from (a.) 0-5 min, (b.) 6-75 min and (c.) absorbance at 550 nm vs. time. Spectra baseline adjusted to give zero absorbance at 800 nm. Data collected at 1 min intervals, initial spectra corresponds to ~15 s after mixing.

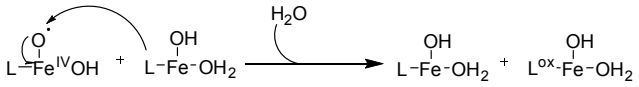

Scheme 2 Possible mechanism for bimolecular inhibition of WO at high concentrations of **2**.

As shown in Fig. 5, at low catalyst concentrations the initial WO rate of **2** is substantially higher than that of **1**. Unlike **1**, **2** shows a brief induction phase of ~20 s (Fig. S32), which may result from slow dissociation of the dimer into monomers upon dilution in the periodate solution. At higher catalyst concentrations, the WO rate of **2** decreases below first order. Taking the value of K_d to be $10^{-3.5}$ (Section 3.1), we find that ~80% of the catalyst is monomeric at a concentration of 83.3 μM, yet the WO rate is only ~40% of that predicted on the basis of a first order fit to the kinetic data. This indicates that in addition to a shift in the dimerization equilibrium towards dimers which are less active for WO, other bimolecular reactions inhibit the WO rate of **2**, such as an increased probability of the high-valent oxyl species oxidizing another nearby species rather than water (Scheme 2).

As shown in Fig. 6, unlike the pH dependence seen for WO by **1**, the WO rate of **2** increases gradually with increasing pH. This suggests deprotonation during or prior to the RDS of WO as is generally found for WOCs.[35,65] The H/D KIE of WO by **2** is 2.6 ± 0.7 at pH 6.0. This secondary KIE indicates that a protonated species is involved in the RDS, but the RDS is not a proton transfer event. Similar KIEs have previously been assigned to rate determining O-O bond formation via the nucleophilic attack of water.[13,66]

Only one peak at ~545 nm is observed in the visible region upon addition of **2** to a solution of sodium periodate (Fig. 16). No charge transfer peak from an oxo-bridged species is observed in the initial solution, indicating that the great majority of **2** is monomeric during the initial phase of the reaction under these conditions. The peak at ~545 nm forms as the WO rate decreases and is similar to that of **C**. The appearance of this peak suggests a similar deactivation pathway for both **1** and **2**, with initial formation of Fe(IV,IV) dimers followed by further decomposition.

3.6 Characterization of Nanoparticles Formed During Reaction of Fe Precursors with Periodate

Because of the recent reports of nanoparticle formation by this family of WOCs,[28,29] we investigated whether iron oxide nanoparticles could serve as an active catalyst for WO under our conditions. No nanoparticle formation is detectable by dynamic light scattering (DLS) upon addition of **1** to a solution of sodium periodate (Fig. S37), although nanoparticles do begin to form after ~25 minutes (Figs. S10 and S38). In contrast, $Fe(NO_3)_3$ rapidly affords nanoparticles upon reaction with periodate (Fig. 17). Despite this rapid nanoparticle formation, no detectable amount of oxygen evolves upon addition of $Fe(NO_3)_3$ to a solution of sodium periodate at pH 5. This result demonstrates that iron oxide nanoparticles do not serve as WOCs under the present reaction conditions. This is in sharp contrast to the WO activity observed for Fe_2O_3 nanoparticles when driven with $Ru(bpy)_3^{2+}/S_2O_8^{2-}$ under more alkaline conditions.[28,29]

In order to explore the reasons for this difference, HAADF-STEM images were obtained, revealing incorporation of iodate or periodate in the nanoparticles formed upon addition of $Fe(NO_3)_3$ to a solution of sodium periodate (Fig. 18). Thus it is possible that this incorporation plays a major role in inhibiting WO by iron oxide nanoparticles. Furthermore, no spectral changes in the visible region are observed during the reaction of $Fe(NO_3)_3$ with sodium periodate, indicating nanoparticle formation does not contribute to the initial spectral changes observed during WO by **1** and **2**.

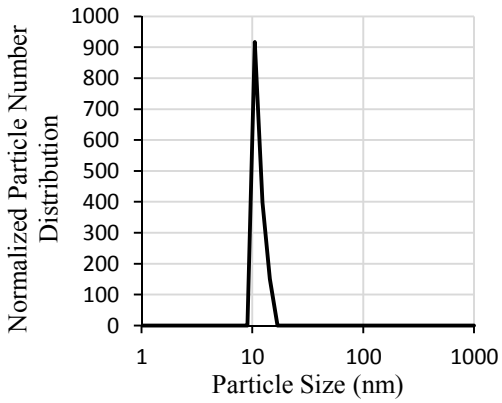

Fig. 17 Nanoparticle size vs. normalized particle number distribution for a solution of 84.7 μM $Fe(NO_3)_3$ upon reaction with 920 μM sodium periodate.

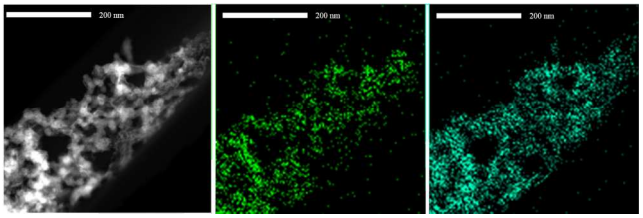

Fig. 18 HAADF-STEM images with elemental maps of nanoparticulate matter formed during the reaction of $Fe(NO_3)_3$ with sodium periodate: HAADF-STEM (left), Fe K-line (middle), I L-line (right). Silicon was also found to be incorporated into the nanoparticles, likely from trace silica present in the reaction solution (Fig. S40).

4. Discussion

4.1 Mechanisms of WO by 1 and 2

Disproportionation of periodate is excluded as a significant contributor to the oxygen production observed on the basis of the saturation kinetics observed for **1** and **2** with respect to periodate concentration (Fig. 4). We can therefore use periodate to obtain insight into the mechanisms of WO by these WOCs. Based on the spectral changes observed during WO by **1** (Fig. 7) and the first order catalyst concentration dependence on the WO rate (Fig. 5), we conclude that the Fe(III,III) μ-oxo-dimer, **A**, is the active species during the initial phase of WO by **1**. As WO by **1** progresses two additional species, **B** and **C**, form with the eventual complete disappearance of the initial catalytic species, **A**. These species are also active WOCs, but are not directly on the catalytic cycle as demonstrated by the differing effects of pH and deuterated solvent on their formation and the observed WO rate (Sections 3.2 and 3.3).

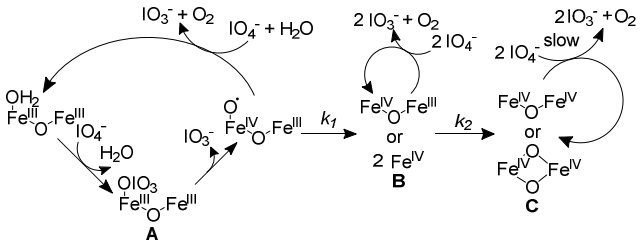

Scheme 3 Summary of species formed during WO by **1**.

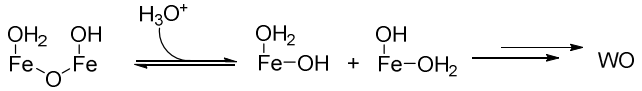

Scheme 4 Proposed equilibrium leading to rate enhancement under acidic conditions observed for **1.**

From the absorption spectral data (Fig. 8) and ESI-MS data (Fig. 14), **C** appears to correspond to either a mono- or bis-μ-oxo-Fe(IV,IV) dimer. The catalyst concentration dependence observed for k_2 suggests that **C** forms via the reaction of two molecules of **B**. In conjunction with the absorption features of **B** (Fig. 8), it is probable that **B** is either an Fe(IV) monomer, an Fe(III,IV) dimer, or a mixture of these two species. **B** was confirmed to be EPR silent in the perpendicular mode, leading to its assignment as an Fe(IV) monomer. However, due to the low concentrations of **B** in the solution, the presence of an Fe(III,IV) dimer cannot be ruled out. The possible chemical species formed during WO by **1** are depicted in Scheme 3.

The rate of WO by **1** shows a clear increase under acidic conditions (Fig. 6). This rate enhancement at low pH is extremely unusual for WOCs, as the RDS in WO is usually either nucleophilic attack by water or oxyl radical coupling,[16] both of which should be inhibited under acidic conditions. Based on the observed secondary inverse KIE (Section 3.2), we may exclude protonation of the complex as the RDS of WO by **1**. An alternative possibility is that species **B**, and potentially species **A**, consists of an equilibrium between monomeric and dimeric species, with the equilibrium shifted toward more active monomers at low pH (Scheme 4). This type of mechanism explains why characterization of **B** has proven challenging. There may be other mechanisms which could lead to the observed rate enhancement at low pH, such as an acid base equilibrium not easily observed in the spectral deconvolutions. A more detailed interpretation of this effect is not available at the moment due to the fact that both **A** and **B** contribute to the observed initial WO rate. Further investigation into the mechanism of WO by **1** is needed in order to confirm the identity of **B** and whether a monomer-dimer equilibrium exists for **A** and **B**.

In contrast to **1**, **2** is ~95% monomeric during WO at 10.55 μM (Section 3.1). As the concentration of **2** is increased dimeric species begin to form in solution (Fig. 3). This dimer formation is accompanied by a decrease in the WO rate, indicating that the monomeric species are more active WOCs than the dimeric species. Dimer formation alone cannot fully explain the observed decrease in the WO rate. Other bimolecular interactions, such as ligand oxidation catalyzed by **2** (Scheme 2), must also interfere with WO at high catalyst concentrations. The H/D KIE and pH dependence observed for **2** suggest that the RDS during WO by **2** is nucleophilic attack of water (Scheme 5),[13,66] as has been

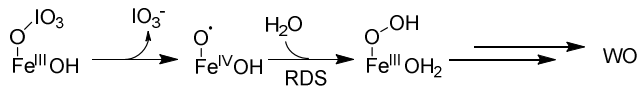

Scheme 5 Proposed mechanism for WO by **2**.

proposed previously for this family of WOCs.[32,33]

It was previously suggested based on calculations that nucleophilic attack of water on related non-heme Fe-based WOCs is a two step process, with initial proton transfer from water followed by nucleophilic attack of the resultant hydroxide on the Fe oxyl, resulting in a KIE of ~1.[32,33] Nevertheless, it was also reported that changes in the reaction geometry could favor a more concerted process, as the calculated energy difference between the deprotonation and nucleophilic attack steps in these studies is within the error of the calculations.[33] In the present study, the difference in reaction conditions and ligand used may therefore sufficiently alter the reaction profile to favor a concerted mechanism.

4.2 Homogeneity versus Heterogeneity when Driven with Periodate

As nanoparticles were demonstrated to serve as WOCs when related catalysts were driven with $Ru(bpy)_3^{2+}/S_2O_8^{2-}$,[28] we investigated whether they could be responsible for the WO observed with sodium periodate. No nanoparticles form upon addition of **1** to sodium periodate during catalytically relevant timescales (Section 3.6). Furthermore, no WO occurs upon addition of $Fe(NO_3)_3$ to a sodium periodate solution, despite rapid nanoparticle formation under these conditions; this demonstrates that iron oxide nanoparticles are not capable of catalyzing WO under these reaction conditions. HAADF-STEM with energy dispersive X-ray analysis reveals poisoning of the nanoparticles by incorporation of iodate or periodate, providing a possible explanation for this behavior (Fig. 18). However, other possibilities, such as inhibition of WO by the nanoparticles due to the low pH, cannot be ruled out. Thus, under the conditions used in this paper, **1** and **2** have been shown to serve as homogeneous WOCs, and nanoparticles do not contribute to the observed WO.

5. Conclusions

By studying the kinetics of WO by **2** as a function of catalyst concentration and pH using sodium periodate, we find it follows a catalytic mechanism similar to that reported for non-heme Fe WOCs when driven with CAN. In this mechanism the RDS of WO is nucleophilic attack of water on a high valent iron oxo or oxyl species. Both monomeric and dimeric complexes of **2** are active catalysts for WO, with the monomer showing higher catalytic activity. Deactivation of **2** occurs via the formation of Fe(IV) dimers. Surprisingly, the mechanism of WO by **1** is significantly more complicated than that of **2**, with the WO rate of **1** increasing with decreasing pH. This pH dependence suggests the presence of a monomer-dimer equilibrium prior to the RDS of WO by **1**. Additionally, WO by **1** involves several species derived from the parent complex. These species correspond to different oxidation states of **1** and are not directly along the catalytic cycle, but rather exist on branch pathways as demonstrated by their H/D KIE values and the effect of pH on their rates of formation. Finally, when driven with sodium periodate, non-heme iron WOCs are homogeneous, and in fact

iron oxide nanoparticles do not serve as WOCs under the conditions reported.

Acknowledgements

This work was partly supported by a Grant-in-Aid for Scientific Research (B) (No. 24350029), a Grant-in-Aid for Scientific Research on Innovative Areas 'Coordination Programming' (No. 2107) (No. 24108732), and a Grant-in-Aid for Scientific Research on Innovative Areas 'Artificial Photosynthesis' (No. 2406) (No. 24107004) from the Ministry of Education, Culture, Sports, Science, and Technology (MEXT) of Japan. This work was further supported by the International Institute for Carbon Neutral Energy Research (WPI-I2CNER), sponsored by the World Premier International Research Center Initiative (WPI), MEXT, Japan.

Abbreviations

BPyA, 1-(Bis(2-methylpyridyl)amino)-2-methyl-2-propanoate. CAN, Cerium(IV) Ammonium Nitrate. CV, Cyclic Voltammogram. KIE, Kinetic Isotope Effect. RDS, Rate-determining Step. TPA, Tris(2-methylpyridyl)amine. WO, Water Oxidation. WOC, Water Oxidation Catalyst.

Notes and references

[a] *International Institute for Carbon-Neutral Energy Research (WPI-I2CNER), Kyushu University, Motooka 744, Nishi-ku, Fukuoka 819-0395, Japan*

[b] *Department of Chemistry, Faculty of Sciences, Kyushu University, 6-10-1 Hakozaki, Higashi-ku, Fukuoka 812-8581, Japan*

[c] *Center for Molecular Systems (CMS), Kyushu University, Motooka 744, Nishi-ku, Fukuoka 819-0395, Japan*

E-mail: aparent@chem.kyushu-univ.jp; ksakai@chem.kyushu-univ.jp

† Electronic Supplementary Information (ESI) available: ESI-MS and NMR data for the starting materials, details of the SPECFIT global fits, figures not included in the main text for brevity, ACF fitting curves from DLS measurements, crystallographic parameters for **1** and **2**. See DOI: 10.1039/b000000x/

1. T. R. Cook, D. K. Dogutan, S. Y. Reece, Y. Surendranath, T. S. Teets, and D. G. Nocera, *Chem. Rev.*, 2010, **110**, 6474–6502.
2. S. Masaoka and K. Sakai, *Chem. Lett.*, 2009, **38**, 182–183.
3. M. Yoshida, S. Masaoka, and K. Sakai, *Chem. Lett.*, 2009, **38**, 702–703.
4. M. Yoshida, S. Masaoka, J. Abe, and K. Sakai, *Chem. – Asian J.*, 2010, **5**, 2369–2378.
5. A. Kimoto, K. Yamauchi, M. Yoshida, S. Masaoka, and K. Sakai, *Chem. Commun.*, 2012, **48**, 239–241.
6. J. J. Concepcion, J. W. Jurss, J. L. Templeton, and T. J. Meyer, *J. Am. Chem. Soc.*, 2008, **130**, 16462–16463.
7. J. A. Gilbert, D. S. Eggleston, W. R. Murphy, D. A. Geselowitz, S. W. Gersten, D. J. Hodgson, and T. J. Meyer, *J. Am. Chem. Soc.*, 1985, **107**, 3855–3864.
8. L. Duan, Y. Xu, P. Zhang, M. Wang, and L. Sun, *Inorg. Chem.*, 2010, **49**, 209–215.
9. L. Duan, F. Bozoglian, S. Mandal, B. Stewart, T. Privalov, A. Llobet, and L. Sun, *Nat. Chem.*, 2012, **4**, 418–423.
10. D. J. Wasylenko, C. Ganesamoorthy, M. A. Henderson, and C. P. Berlinguette, *Inorg. Chem.*, 2011, **50**, 3662–3672.
11. S. Maji, I. López, F. Bozoglian, J. Benet-Buchholz, and A. Llobet, *Inorg. Chem.*, 2013, **52**, 3591–3593.
12. D. E. Polyansky, J. T. Muckerman, J. Rochford, R. Zong, R. P. Thummel, and E. Fujita, *J. Am. Chem. Soc.*, 2011, **133**, 14649–14665.
13. J. D. Blakemore, N. D. Schley, D. Balcells, J. F. Hull, G. W. Olack, C. D. Incarvito, O. Eisenstein, G. W. Brudvig, and R. H. Crabtree, *J. Am. Chem. Soc.*, 2010, **132**, 16017–16029.
14. J. D. Blakemore, N. D. Schley, G. W. Olack, C. D. Incarvito, G. W. Brudvig, and R. H. Crabtree, *Chem Sci*, 2011, 94–98.
15. J. Limburg, J. S. Vrettos, L. M. Liable-Sands, A. L. Rheingold, R. H. Crabtree, and G. W. Brudvig, *Science*, 1999, **283**, 1524 –1527.
16. D. J. Wasylenko, R. D. Palmer, and C. P. Berlinguette, *Chem. Commun.*, 2013, **49**, 218–227.
17. K. J. Young, L. A. Martini, R. L. Milot, R. C. Snoeberger III, V. S. Batista, C. A. Schmuttenmaer, R. H. Crabtree, and G. W. Brudvig, *Coord. Chem. Rev.*, 2012, **256**, 2503–2520.
18. M. W. Kanan and D. G. Nocera, *Science*, 2008, **321**, 1072 –1075.
19. Q. Yin, J. M. Tan, C. Besson, Y. V. Geletii, D. G. Musaev, A. E. Kuznetsov, Z. Luo, K. I. Hardcastle, and C. L. Hill, *Science*, 2010, **328**, 342 –345.
20. D. K. Dogutan, R. McGuire, and D. G. Nocera, *J. Am. Chem. Soc.*, 2011, **133**, 9178–9180.
21. T. Nakazono, A. R. Parent, and K. Sakai, *Chem. Commun.*, 2013, 6325–6327.
22. Y. Naruta, M. Sasayama, and T. Sasaki, *Angew. Chem. Int. Ed. Engl.*, 1994, **33**, 1839–1841.
23. Y. Shimazaki, T. Nagano, H. Takesue, B.-H. Ye, F. Tani, and Y. Naruta, *Angew. Chem. Int. Ed.*, 2004, **43**, 98–100.
24. W. M. C. Sameera, C. J. McKenzie, and J. E. McGrady, *Dalton Trans.*, 2011, **40**, 3859–3870.
25. M. Wiechen, H.-M. Berends, and P. Kurz, *Dalton Trans.*, 2011, **41**, 21–31.
26. W. C. Ellis, N. D. McDaniel, S. Bernhard, and T. J. Collins, *J. Am. Chem. Soc.*, 2010, **132**, 10990–10991.
27. J. Lloret-Fillol, Z. Codolà, I. Garcia-Bosch, L. Gómez, J. J. Pla, and M. Costas, *Nat Chem*, 2011, **3**, 807–813.
28. G. Chen, L. Chen, S.-M. Ng, W.-L. Man, and T.-C. Lau, *Angew. Chem. Int. Ed.*, 2013, **52**, 1789–1791.
29. D. Hong, S. Mandal, Y. Yamada, Y.-M. Lee, W. Nam, A. Llobet, and S. Fukuzumi, *Inorg. Chem.*, 2013, **52**, 9522–9531.
30. B. Zhang, F. Li, F. Yu, H. Cui, X. Zhou, H. Li, Y. Wang, and L. Sun, *Chem. – Asian J.*, 2014, **9**, 1515–1518.
31. E. E. Kasapbasi and M.-H. Whangbo, *Inorg. Chem.*, 2012, **51**, 10850–10855.
32. Z. Codolà, I. Garcia-Bosch, F. Acuña-Parés, I. Prat, J. M. Luis, M. Costas, and J. Lloret-Fillol, *Chem. – Eur. J.*, 2013, **19**, 8042–8047.
33. F. Acuña-Parés, Z. Codolà, M. Costas, J. M. Luis, and J. Lloret-Fillol, *Chem. – Eur. J.*, 2014, **20**, 5696–5707.
34. M. M. Najafpour, A. N. Moghaddam, D. J. Sedigh, and M. Hołyńska, *Catal. Sci. Technol.*, 2013, **4**, 30–33.
35. A. R. Parent, J. D. Blakemore, G. W. Brudvig, and R. H. Crabtree, *Chem Commun*, 2011, **47**, 11745–11747.
36. A. R. Parent, T. P. Brewster, W. De Wolf, R. H. Crabtree, and G. W. Brudvig, *Inorg. Chem.*, 2012, **51**, 6147–6152.
37. U. Hintermair, S. M. Hashmi, M. Elimelech, and R. H. Crabtree, *J. Am. Chem. Soc.*, 2012, **134**, 9785–9795.
38. A. Savini, A. Bucci, G. Bellachioma, L. Rocchigiani, C. Zuccaccia, A. Llobet, and A. Macchioni, *Eur. J. Inorg. Chem.*, 2014, **2014**, 690–697.
39. A. Lewandowska-Andralojc, D. E. Polyansky, C.-H. Wang, W.-H. Wang, Y. Himeda, and E. Fujita, *Phys. Chem. Chem. Phys.*, 2014.
40. A. J. Ingram, A. B. Wolk, C. Flender, J. Zhang, C. J. Johnson, U. Hintermair, R. H. Crabtree, M. A. Johnson, and R. N. Zare, *Inorg. Chem.*, 2014, **53**, 423–433.
41. W. A. Hoffert, M. T. Mock, A. M. Appel, and J. Y. Yang, *Eur. J. Inorg. Chem.*, 2013, **2013**, 3846–3857.
42. Z. Codolà, J. M. S. Cardoso, B. Royo, M. Costas, and J. Lloret-Fillol, *Chem. – Eur. J.*, 2013, **19**, 7203–7213.
43. A. R. Parent, R. H. Crabtree, and G. W. Brudvig, *Chem. Soc. Rev.*, 2013, **42**, 2247–2252.
44. D. G. H. Hetterscheid and J. N. H. Reek, *Eur. J. Inorg. Chem.*, 2014, **2014**, 742–749.
45. SPECFIT; Spectrum Research Associate: Chapel Hill, NC
46. K. Sakai, *WinMassSpec*, Kyushu University, Fukuoka City, Japan.

47. Roger Gordon Bates, *Determination of pH: Theory and Practice*, Wiley, New York, 2nd edn., 1964.
48. J. T. Groves and I. O. Kady, *Inorg. Chem.*, 1993, **32**, 3868–3872.
49. G. M. Sheldrick, *SADABS*, Bruker AXS Inc., Madison, WI USA, 1997.
50. G. M. Sheldrick, *SHELXS-97, Program for solution of crystal structures*, University of Gottingen, Germany, 1997.
51. G. M. Sheldrick, *SHELXL-97, Program for refinement of crystal structures*, University of Gottingen, Germany, 1997.
52. C. K. Johnson, *ORTEPII*, Oak Ridge National Laboratory, Tennessee, USA, 1976.
53. *TEXSAN*, Molecular Structure Coporation, MSC, 3200 Research Forest Drive, The Woodlands, TX 77381, USA, 2001.
54. C. M. Smith and R. E. Norman, *Acta Crystallogr. Sect. E Struct. Rep. Online*, 2007, **63**, m2480–m2481.
55. G. L. Parrilha, C. Fernandes, A. J. Bortoluzzi, B. Szpoganicz, M. de S. Silva, C. T. Pich, H. Terenzi, and A. Horn Jr., *Inorg. Chem. Commun.*, 2008, **11**, 643–647.
56. L. H. Do, G. Xue, L. Que, and S. J. Lippard, *Inorg. Chem.*, 2012, **51**, 2393–2402.
57. K. W. Jennette, J. T. Gill, J. A. Sadownick, and S. J. Lippard, *J. Am. Chem. Soc.*, 1976, **98**, 6159–6168.
58. X. Sala, S. Maji, R. Bofill, J. García-Antón, L. Escriche, and A. Llobet, *Acc. Chem. Res.*, 2014, **47**, 504–516.
59. F. Liu, J. J. Concepcion, J. W. Jurss, T. Cardolaccia, J. L. Templeton, and T. J. Meyer, *Inorg. Chem.*, 2008, **47**, 1727–1752.
60. D. C. Marelius, S. Bhagan, D. J. Charboneau, K. M. Schroeder, J. M. Kamdar, A. R. McGettigan, B. J. Freeman, C. E. Moore, A. L. Rheingold, A. L. Cooksy, D. K. Smith, J. J. Paul, E. T. Papish, and D. B. Grotjahn, *Eur. J. Inorg. Chem.*, 2014, **2014**, 676–689.
61. J. Bautz, M. R. Bukowski, M. Kerscher, A. Stubna, P. Comba, A. Lienke, E. Münck, and L. Que, *Angew. Chem. Int. Ed.*, 2006, **45**, 5681–5684.
62. P. Comba, G. Rajaraman, and H. Rohwer, *Inorg. Chem.*, 2007, **46**, 3826–3838.
63. A. Company, Y. Feng, M. Güell, X. Ribas, J. M. Luis, L. Que, and M. Costas, *Chem. – Eur. J.*, 2009, **15**, 3359–3362.
64. T. Jüstel, M. Müller, T. Weyhermüller, C. Kressl, E. Bill, P. Hildebrandt, M. Lengen, M. Grodzicki, A. X. Trautwein, B. Nuber, and K. Wieghardt, *Chem. – Eur. J.*, 1999, **5**, 793–810.
65. S. J. Raven and T. J. Meyer, *Inorg. Chem.*, 1988, **27**, 4478–4483.
66. Z. Chen, J. J. Concepcion, X. Hu, W. Yang, P. G. Hoertz, and T. J. Meyer, *Proc. Natl. Acad. Sci.*, 2010, **107**, 7225–7229.

Non-heme iron complexes were determined to serve as homogeneous water oxidation catalysts when driven with sodium periodate. Both mononuclear and dinuclear complexes were found to be active for water oxidation, with the monomeric species exhibiting higher rates.